Physics-informed Neural ODE for Post-disaster Mobility Recovery

Jiahao Li*
Shenzhen International Graduate
School, Tsinghua University
Shenzhen, China
li-jh23@mails.tsinghua.edu.cn

Huandong Wang*
Department of Electronic
Engineering, Tsinghua University
Beijing, China
wanghuandong@tsinghua.edu.cn

Xinlei Chen[†]
Shenzhen International Graduate
School, Tsinghua University
Pengcheng Laboratory
RISC-V International Open Source
Laboratory
Shenzhen, China
chen.xinlei@sz.tsinghua.edu.cn.

ABSTRACT

Urban mobility undergoes a profound decline in the aftermath of a disaster, subsequently exhibiting a complex recovery trajectory. Effectively capturing and predicting this dynamic recovery process holds paramount importance for devising more efficient post-disaster recovery strategies, such as resource allocation to areas with protracted recovery periods. Existing models for post-disaster mobility recovery predominantly employ basic mathematical methods, which are strongly based on simplifying assumptions, and their limited parameters restrict their capacity to fully capture the mobility recovery patterns. In response to this gap, we introduce the Coupled Dynamic Graph ODE Network (CDGON) to model the intricate dynamics of post-disaster mobility recovery. Our model seamlessly integrates existing physical knowledge pertaining to post-disaster mobility recovery and incorporates the nuanced interactions between intra-regional and inter-regional population flows. Extensive experimental results demonstrate the efficiency of our model in capturing the dynamic recovery patterns of urban population mobility in post-disaster scenarios, surpassing the capabilities of current dynamic graph prediction models.

CCS CONCEPTS

• **Networks** → *Network dynamics*; • **Computing methodologies** → **Machine learning algorithms**; • **Human-centered computing** → *Social engineering (social sciences).*

KEYWORDS

Physics-informed; Graph Neural ODE; Urban Mobility Recovery; Post-Disaster

---

*Both authors contributed equally to this research.
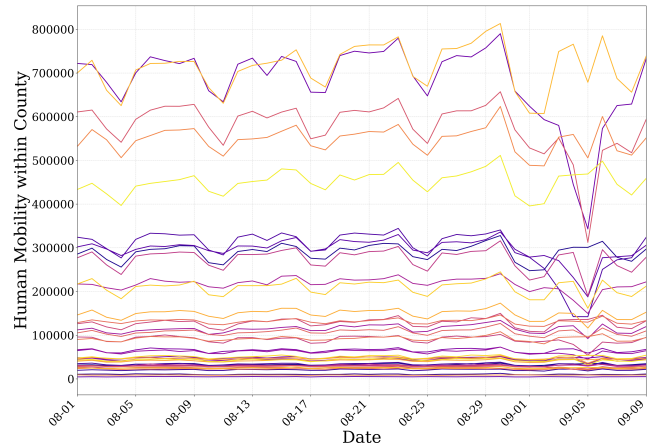[†]Corresponding author.

Figure 1: Human mobility within each county over time in South Carolina, where a line represents the intra-regional population flow curve of a county, and different colors represent different counties.

1 INTRODUCTION

The fast progress of urbanization and frequently occurred extreme events (disasters) around the world have caused a non-negligible impact on the lives and safety of urban residents [14]. As a result, there is an urgent need to have a deep understanding of urban resilience, i.e., the ability of the city to rapidly recover its functionalities from the shock of extreme events, where human mobility within urban areas has played a critical role [23, 44]. On the one hand, urban mobility reflects the behaviors of urban residents in terms of traveling from residential areas to other functional areas to acquire essential resources (e.g., food and money), thus serving as a pivotal indicator of residents' satisfaction with access to necessities [23]. On the other hand, urban mobility is intricately linked with the normal operation of urban infrastructures, e.g., transport facilities and office buildings, thus reflecting the recovery status of urban infrastructures [44]. Less resilient cities often need more time to resume normal urban mobility, thereby causing greater impacts on the lives of urban residents and more economic losses. Thus, accurately predicting the recovery process of urban mobility after disasters helps to detect high-risk urban communities, design better emergency response strategies, and ultimately build a more intelligent and resilient city [39].

However, predicting the post-disaster recovery process of urban mobility is also a difficult task with the following challenges. Firstly, the post-disaster recovery of urban mobility has complicated patterns intricately intertwined with diverse disaster situations and their normal mobility characteristics before disasters [20, 38, 47]. For instance, as depicted in Fig. 1, the temporal recovery curves of human mobility in different regions, i.e., counties in this instance, of South Carolina after Hurricane Dorian in September 2019 exhibit significant diversity and notable fluctuations. These phenomena are largely caused by complicated disaster situations in different regions, coupled with the inherent diversity in their normal mobility features before disasters. However, the underlying mechanisms remain unclear and are difficult to be accurately modeled just using observable data. Secondly, the recovery processes of different urban areas are interdependent. Interactions between regions, which can be characterized by inter-regional population flows, have significant influences on their recovery processes. Urban areas with larger net population inflow will have a quicker recovery rate, as they have a larger active population, thereby facilitating the reconstruction and recovery process [43]. These interactions between regions are also highly dynamic and further amplify the complexity of effectively modeling and predicting their dynamics [11].

However, existing approaches for modeling the post-disaster recovery process of urban mobility are mainly model-based methods [23, 38, 43]. They make strong simplifying assumptions about urban mobility, and then employ mathematical models constructed with a limited number of parameters with explicit physical interpretations to fit its recovery process [23, 38, 43]. For example, Li et al. [23] propose a hyperbolic model, which is called the spatiotemporal decay model, to describe the temporal recovery patterns of urban mobility. Yabe et al. [43] developed two coupled differential equation models to describe the recovering dynamics of the sociophysical system composed of physical infrastructure and urban mobility. Although these models provide valuable knowledge about the recovery of post-disaster urban mobility, strong simplifying assumptions and limited model parameters restrict their capacity to fully capture the diverse and complicated recovery patterns of post-disaster urban mobility. Moreover, all these models fail to effectively model the influence of inter-regional population flows on their recovery.

At the same time, the rapid development of data-driven deep learning technologies, represented by graph neural networks (GNN) and neural ordinary differential equations (Neural ODE) [18, 50], has equipped us with enhanced capabilities to model the dynamics of co-evolved nodes and edges in graph structures. Furthermore, the rise of physics-informed machine learning facilitates the integration of prior physical knowledge into data-driven modeling frameworks [42]. These methodologies present a promising solution for effectively modeling and predicting post-disaster urban mobility dynamics in the data-driven paradigm.

In this paper, we propose a deep learning framework, named Coupled Dynamic Graph ODE Network (CDGON), to predict the recovery process of post-disaster urban mobility. To overcome the first challenge, we employ a paradigm of physics-inspired machine learning to construct a neural ODE function guided by the spatiotemporal decay model. It enables effective modeling of the diverse and highly fluctuating urban mobility within different regions, and

jointly considers urban mobility before and after disasters. Further, we introduce another set of coupled neural ODE functions to describe the dynamics of inter-regional population flows, which serve as edges in the formed dynamic graph to characterize the complicated post-disaster urban mobility. The two sets of neural ODE functions jointly model the co-evolving process of nodes and edges in the dynamic graph in terms of intra-regional and inter-regional population flow, thus effectively solving the second challenge. Overall, our contributions can be summarized as follows:

- We integrate the physics-based knowledge from the spatiotemporal decay model into the neural ODE model, and derive a powerful framework for capturing the intertwined dynamics of urban mobility before and after disasters.
- We employ coupled neural ODE functions to jointly model the co-evolving process of intra-regional and inter-regional population flow, capturing dynamic interactions between regions in the post-disaster recovery process.
- Extensive experimental results demonstrate the efficiency of our model in capturing the dynamic recovery patterns of urban mobility in post-disaster scenarios, surpassing the capabilities of current dynamic graph prediction models.

2 PRELIMINARIES

2.1 Spatiotemporal Decay Model (ST Decay Model)

In this section, we introduce the Spatiotemporal Decay Model (ST Decay Model) proposed by Li et al. [23]. This model is formulated as a hyperbolic equation, represented as follows:

$$r_i(t) = \frac{\overline{r_i}}{1 + k(t)\sum_{j=1}^{L} w_{ij}N_j(t)}, \tag{1}$$

where $r_i(t)$ denotes the abnormal mobility in region i after a disaster, and $\overline{r_i}$ represents the normal mobility of region i prior to the disaster. Eq. (1) illustrates that abnormal urban mobility after disasters tends to normalize over time, attributable to the reduction in the value of $k(t)\sum_{j=1}^{L} w_{ij}N_j(t)$. In this context, $k(t)$ measures temporal decay, capturing the decline in mobility behavior changes over time, while $\sum_{j=1}^{L} w_{ij}N_j(t)$ measures spatial decay. Here, $N_j(t)$ denotes the severity of the crisis in the region j at time t, where region j is a neighbor of the region i, and w_{ij} represents the spatial weight between i and j.

Specifically, the temporal decay function $k(t)$ is best described by the negative exponential function $k_0 e^{-\alpha t}$ [23] as follows:

$$k(t) = k_0 e^{-\alpha t}, \tag{2}$$

where α serves as the parameter that governs the rate of decay, and k_0 represents the initial rate of change in mobility behavior.

2.2 Graph Neural ODE

Neural Ordinary Differential Equation (Neural ODE) is a type of deep neural network introduced by Chen et al. [3], which merges the neural networks with ordinary differential equations, offering a continuous generalization of the Residual Neural Network (ResNet) [15]. Neural ODE facilitates the seamless incorporation of neural networks for continuously learning residuals, thereby endowing it with robust fitting capabilities. Poli et al. [29] integrate

Graph Convolutional Networks (GCN) into Neural ODE. Following this work, numerous studies incorporate GCN into Neural ODE for dynamic graph prediction [12, 18, 50], which is one of the most challenging tasks in graph learning. The equation of graph Neural ODE can be described as follows:

$$Z^T = Z^0 + \int_{t=0}^{t=T} f_G(Z^t, \Theta) dt, \tag{3}$$

where Z^0 represents the node embeddings in a graph at the initial moment, and f_G is a function designed for processing nodes embeddings with learnable parameters Θ. Here, f_G is often replaced with a graph convolution operation. Integration across the interval $[0, T]$ yields Z^T, denoting the node embeddings at time T.

3 PROBLEM FORMULATION

The discrete dynamic population mobility graph sequence is defined as $\mathcal{G} = \{G^0, G^1, \ldots, G^T\}$, where $G^t = (\mathcal{V}, \mathcal{E}^t, X^t, A^t)$ is a human mobility graph with $\mathcal{V}$ denoting the set of n regions, which is treated as nodes. The feature matrix at timestamp t is represented as X^t. The set $\mathcal{E}^t$ indicates the population flows between different regions at timestamp t, which is treated as edges, with their features forming the weighted adjacency matrix A^t at timestamp t.

Since population mobility recovers day by day instead of hour by hour, thus G^t denotes the population mobility on day t. The related definitions of the features on nodes and edges are as follows:

DEFINITION 1 (INTRA-REGIONAL POPULATION FLOW). *The intra-regional population flow within region $i \in \mathcal{V}$ at day t is denoted as $x_i^t \in \mathbb{R}$. This node feature measures the total population that moved within this region, representing the population mobility of region i. Consequently, the feature matrix of nodes at day t is $X^t \in \mathbb{R}^{N \times 1}$, with its dynamic sequence represented as $X = \{X^0, X^1, \ldots, X^T\}$.*

DEFINITION 2 (INTER-REGIONAL POPULATION FLOW). *The inter-regional population flow from region i to region j at day t is denoted as $x_{ij}^t \in \mathbb{R}$. This feature on edge $e_{ij}^t \in \mathcal{E}^t$ calculates the volume of the population that moves from region i to region j at day t and represents the population mobility between these two regions. Therefore, the corresponding weighted adjacent matrix sequence is $\mathcal{A} = \{A^0, A^1, \ldots, A^T\}$ where the element in the ith row and jth column of A^t is x_{ij}^t.*

In the realm of dynamic graph prediction, traditional methods typically leverage historical graph sequences to predict future graphs, performing well under normal circumstances as population mobility tends to fluctuate periodically within a predictable range. However, the occurrence of a disaster disrupts this regular pattern, leading to a shift in population mobility towards an abnormal state. Consequently, historical population mobility patterns prior to the disaster become inadequate for predicting the mobility recovery process under abnormal conditions.

To address this challenge, letting $\mathcal{G}$ represent the sequence of abnormal population mobility graphs during the recovery process, with the landfall day of the disaster as the initial moment, we define a normal population mobility graph to guide the abnormal mobility recovery as follows:

DEFINITION 3 (NORMAL POPULATION MOBILITY GRAPH). *The normal population mobility graph is defined as $\overline{G} = (\mathcal{V}, \mathcal{E}^t, \overline{X}, \overline{A})$, where the normal intra-regional population flow matrix is $\overline{X} = $*

$\frac{1}{T_1 - T_2} \sum_{t=T_1}^{t=T_2} X^t$ *and the normal weighted adjacent matrix is $\overline{A} = \frac{1}{T_1 - T_2} \sum_{t=T_1}^{t=T_2} A^t$. Here, T_1 and T_2 are the starting and ending days of a normal period before a disaster.*

We now define the post-disaster dynamic population mobility graph prediction problem as follows:

DEFINITION 4 (POST-DISASTER DYNAMIC POPULATION MOBILITY GRAPH PREDICTION PROBLEM). *Given the initial abnormal population mobility graph G^0 and normal population mobility graph $\overline{G}$, predict the subsequent population mobility graphs $G^t, t \in \{1, 2, \ldots, T\}$ during the recovery process after the disaster.*

4 METHODOLOGY

4.1 Framework of Proposed Method

The goal of our Coupled Dynamic Graph ODE Network (CDGON) is to predict the population mobility recovery process post-disaster using the initial abnormal population mobility graph and the normal population mobility graph, which is challenging since the available data is limited. To address this difficulty, we leverage the prior physical knowledge derived from the ST Decay Model to design our node ODE function and carefully model the co-evolution of nodes and edges, effectively solving the post-disaster dynamic population mobility graph prediction problem.

Fig. 2 presents an overview of our model architecture, comprising the Encoder, the ST Decay Model Informed Neural ODE, and the Decoder. The Encoder first maps the initial abnormal population mobility graph and normal intra-regional population flow into a latent space. Then, the ST Decay Model Informed Neural ODE captures the dynamic of the mobility recovery. Finally, the Decoder generates the predictive graph and filters out unreasonable results.

4.2 Encoder for Population Mobility Graph

To initiate the modeling process, the initial abnormal intra-regional population flows x_i^0 within nodes and corresponding normal intra-regional population flows $\overline{x_i}$ are jointly encoded through an identical node encoder $F_{EncN} : \mathbb{R}^1 \to \mathbb{R}^d$ as follows:

$$z_i^0 = F_{EncN}(x_i^0), \tag{4}$$

$$\overline{z_i} = F_{EncN}(\overline{x_i}), \tag{5}$$

where z_i^0 and $\overline{z_i}$ are both d-dimensional vectors.

Additionally, the initial abnormal inter-regional population flows x_{ij}^0 on edges are encoded through the edge encoder $F_{EncE} : \mathbb{R}^1 \to \mathbb{R}^d$, producing the edge latent state z_{ij}^0, which is also a d-dimensional vector:

$$z_{ij}^0 = F_{EncE}(x_{ij}). \tag{6}$$

4.3 ST Decay Model Informed Neural ODE

After acquiring the initial state of node z_i^0 and edge z_{ij}^0, our ST Decay Model Informed Neural ODE utilizes them to generate the subsequent latent states $z_i^1, z_i^2, \ldots, z_i^T$ for nodes and $z_{ij}^1, z_{ij}^2, \ldots, z_{ij}^T$ for edges, where T is the observed recovery time length. Notably, this generation process is guided by the latent state of normal intra-regional mobility $\overline{z_i}$.
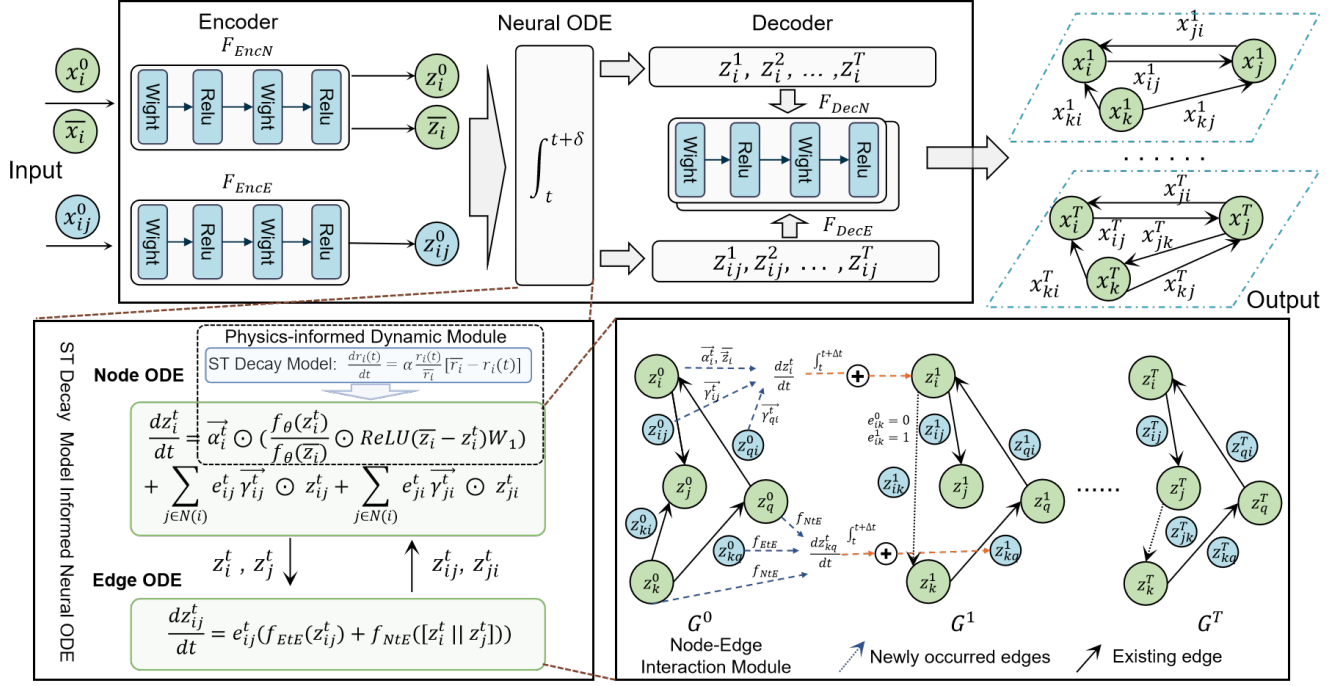
Figure 2: Model architectrue.

This section introduces two primary components of our ST Decay Model Informed Neural ODE: the Physics-informed Dynamic Module (PIDM) and the Node-Edge Interaction Module (NEIM).

4.3.1 Physics-informed Dynamic Module. Before we delve into our PIDM, we first introduce the theorem that is deduced from the ST Decay Model:

Theorem 1. *Denote $r_i(t)$ as the abnormal intra-regional population flow of region i after a disaster, which is described in the ST Decay Model shown in Eq. (1). The derivative of $r_i(t)$ satisfies the following differential equation:*

$$\frac{\mathrm{d}r_i(t)}{\mathrm{d}t} = \alpha \frac{r_i(t)}{\overline{r_i}}[\overline{r_i} - r_i(t)], \tag{7}$$

where α indicates the decay coefficient. It implies that $r_i(t)$ will approach to the normal intra-regional population flow $\overline{r_i}$ over time governed by α.

Proof. See the Appendix for proof. □

Eq. (7) in **Theorem 1** describes the self-evolution of intra-regional population flow in the region i. Therefore, it can inform the design of our node ODE function. However, Eq. (7) describes the 1-dimensional dynamics of mobility recovery. Modeling this in a d-dimensional space requires a well-designed network structure.

Consequently, we proposed PIDM, structurally resembling Eq. (7), to capture the self-evolution of the node latent state. The module is depicted as follows:

$$\frac{\mathrm{d}z_i^t}{\mathrm{d}t} = \vec{\alpha}_i^t \odot (\frac{f_\theta(z_i^t)}{f_\theta(\overline{z_i})} \odot ReLU(\overline{z_i} - z_i^t)W_1), \tag{8}$$

where $\odot$ indicates the element-wise product, and $\vec{\alpha}_i^t \in \mathbb{R}^d$ represents the decay coefficient vector for region i, analogous to the parameter α in Eq. (7), which means we calculate a decay parameter for each element in the hidden state vector.

Given that the true values of population mobility can reach several million for regions with large populations, a potential numerical explosion might occur for the term $(z_i^t)^2$ in $\frac{z_i^t}{\overline{z_i}}[\overline{z_i} - z_i^t]$ if we design the node ODE directly as in Eq. (7). Therefore, we replace $\frac{z_i^t}{\overline{z_i}} \in \mathbb{R}^d$ with $\frac{f_\theta(z_i^t)}{f_\theta(\overline{z_i})} \in \mathbb{R}^1$, where $f_\theta : \mathbb{R}^d \rightarrow \mathbb{R}^1$ calculates a scalar from a d-dimensional vector, helping to avoid the potential numerical explosion problem. While $\overline{z_i} - z_i^t$ remains unchanged, analogous to $\overline{r_i} - r_i(t)$, but we also use a *ReLU* and a learnable transformation matrix $W_1 \in \mathbb{R}^{d \times d}$ to enhance the model's learning capacity.

4.3.2 Node-Edge Interaction Module (NEIM). With the development of our PIDM, it is imperative to acknowledge that, in reality, intra-regional population flow within a region is influenced by inter-regional population flows from other regions [47]. Particularly after a disaster, people who sought refuge in distant areas will return to their original locations. This surge in population inflow leads to a rapid recovery of intra-regional flow in urban areas near the disaster center, especially in cities with large populations. Therefore, considering the interaction between nodes and edges is crucial.

Notably, although the initial edge information is known, the population mobility graph structure is dynamic, meaning edges may vanish or emerge during the evolution. To capture this dynamic,

we compute an adaptive graph weight adjacent matrix $\hat{A}^t$:

$$\hat{A}^t = [a_{ij}^t]_{n \times n}, \tag{9}$$

$$a_{ij}^t = ReLU(g_{EtV}(g_{NtE}([z_i^t \| z_j^t]))), \tag{10}$$

where $\|$ denotes the horizontal concatenation, and a_{ij}^t in the ith row and jth column of $\hat{A}^t$ is learned from the concatenation of the two corresponding nodes through $g_{NtE} : \mathbb{R}^{2d} \rightarrow \mathbb{R}^d$ and $g_{EtV} : \mathbb{R}^d \rightarrow \mathbb{R}^1$. Besides, the $ReLU$ activation function is used to eliminate the negative values.

After $\hat{A}^t$ is generated, drawing inspiration from Coupled Graph ODE [18], we design the edge ODE function as follows:

$$\frac{dz_{ij}^t}{dt} = \hat{e}_{ij}^t[f_{EtE}(z_{ij}^t) + f_{NtE}([z_i^t \| z_j^t])], \tag{11}$$

where $f_{EtE} : \mathbb{R}^d \rightarrow \mathbb{R}^d$ computes the self-evolution of edges, and $f_{NtE} : \mathbb{R}^{2d} \rightarrow \mathbb{R}^d$ captures information from the concatenation of the two connected nodes. Both f_{EtE} and f_{NtE} are linear layers. Specifically, the edge indicator $\hat{e}_{ij}^t$ denotes the connectivity of node i and node j based on a_{ij}^t:

$$\hat{e}_{ij}^t = \begin{cases} 1, & \text{if } a_{ij}^t \geq 1 \\ 0, & \text{if } a_{ij}^t < 1 \end{cases} \tag{12}$$

where $\hat{e}_{ij}^t$ will be 1 if a_{ij}^t exceeds 1, indicating that population flow from region i to region j exists and the edge should be updated.

For the original node ODE function in PIDM, instead of aggregating neighbor information as in [18], we aggregate edges surrounding the node:

$$\frac{dz_i^t}{dt} = \vec{\alpha}_i^t \odot \left(\frac{f_\theta(z_i^t)}{f_\theta(\overline{z_i})} \odot ReLU(\overline{z_i} - z_i^t)W_1 \right) + \sum_{j \in N(i)} \hat{e}_{ij}^t \vec{\gamma}_{ij}^t \odot z_{ij}^t + \sum_{j \in N(i)} \hat{e}_{ji}^t \vec{\gamma}_{ji}^t \odot z_{ji}^t, \tag{13}$$

where $N(i)$ represents all nodes in the graph except for node i, and $\hat{e}_{ij}^t$ detects whether the edge exists. Additionally, the parameter $\vec{\gamma}_{ij}^t \in \mathbb{R}^d$ is used to control the degree of aggregation.

Since the recovery rate of the intra-regional population flow differs for each region, we allocate different decay coefficients $\vec{\alpha}_i^t$ for each region. Moreover, the recovery rate of a region not only depends on itself but also depends on its neighbors. For example, two regions suffering similar damage will recover at different rates if one has healthier neighbors. Consequently, we employ graph convolution to infer $\vec{\alpha}_i^t$ based on the adaptive graph weight adjacent matrix $\hat{A}^t$:

$$[\vec{\alpha}_1^t, \vec{\alpha}_2^t, ..., \vec{\alpha}_n^t]^T = \frac{h_\alpha(\hat{D}^{-1/2}\hat{A}^t\hat{D}^{-1/2}Z^tW)}{max(|h_\alpha(\hat{D}^{-1/2}\hat{A}^t\hat{D}^{-1/2}Z^tW)|)}, \tag{14}$$

where $\hat{D}^{-1/2}$ is the degree matrix of $\hat{A}^t$, and $Z^T = [z_1^t, z_2^t, \ldots, z_n^t]^T$ represents the graph signals composed of all latent node states. After performing graph convolution, a linear layer h_α is applied. While it is common to normalize each value of $\vec{\alpha}_i^t$ into the range [0,1] to indicate a recovery trend, we observe that, in Fig. 1, some counties face a decline shortly in just one or two days after the Dorian for uncertain reasons, which can be subsequent effects of the disaster or the arrival of the workday. Therefore, absolute maximum

normalization is applied to normalize the result to the range [-1,1] instead of [0,1], allowing the model to capture both the rising and falling during recovery.

Equally important, the population inflow to a region might not always promote recovery of this region, as some people who just arrived might leave on the next day for various reasons. Similarly, the population outflow from a region might not necessarily damage the recovery process. Hence, we do not directly add edge states to the node state but use a linear layer h_γ to infer $\vec{\gamma}_{ij}^t$, which controls the influence of an edge to a node:

$$\vec{\gamma}_{ij}^t = Softmax(h_\gamma(z_{ij}^t)), \tag{15}$$

where the $Softmax$ activation function is used.

Once our ordinary differential equations for node $\frac{dz_i^t}{dt}$ and edge $\frac{dz_{ij}^t}{dt}$ are obtained, given the initial node embedding z_i^0 and edge embedding z_{ij}^0, we can generate subsequent latent states of intra-regional and inter-regional population flow using a Neural ODE solver. This process involves repeated integration at equidistant intervals $\triangle t$, where each integration is performed based on the previous integration result:

$$z_i^{t+\triangle t} = z_i^t + \int_t^{t+\triangle t} \frac{dz_i^t}{dt}dt, \tag{16}$$

$$z_{ij}^{t+\triangle t} = z_{ij}^t + \int_t^{t+\triangle t} \frac{dz_{ij}^t}{dt}dt. \tag{17}$$

4.4 Decoder for Population Mobility Graph

Finally, the node decoder $F_{DecN} : \mathbb{R}^d \rightarrow \mathbb{R}^1$ and edge decoder $F_{DecE} : \mathbb{R}^d \rightarrow \mathbb{R}^1$ generate the ultimate predictive outputs for nodes and edges on the corresponding day t:

$$\hat{x}_i^t = F_{DecN}(z_i^t), \tag{18}$$

$$\hat{x}_{ij}^t = e_{ij}^t F_{DecE}(z_{ij}^t), \tag{19}$$

where the use of e_{ij}^t ensures consistency with the network structure during the integration process. Since $\hat{x}_{ij}^t$ represents the absolute value of the predicted inter-regional population flow, it is treated as non-existent if its value is less than 1. Thus, the filtering process is defined as:

$$\hat{x}_{ij}^t = \begin{cases} \hat{x_{ij}}^t, & \text{if } \hat{x_{ij}}^t \geq 1 \\ 0. & \text{if } \hat{x_{ij}}^t < 1 \end{cases} \tag{20}$$

4.5 Model Optimization

Our objective is to minimize the prediction error of population mobility recovery, for which we use the following loss function:

$$\mathcal{L} = \sqrt{\frac{1}{n \times T} \sum_{t=1}^{T} \sum_{i=1}^{n} (x_i^t - \hat{x}_i^t)^2} + \lambda \sqrt{\frac{1}{n \times n \times T} \sum_{t=1}^{T} \sum_{i=1}^{n} \sum_{j=1}^{n} (x_{ij}^t - \hat{x}_{ij}^t)^2}, \tag{21}$$

which calculates the weighted sum of root-mean-square errors (RMSE) between the predicted value $\hat{x}_i^t$, $\hat{x}_{ij}^t$ and the true value x_i^t,

Table 1: The life of Hurricane Dorian (2019).

Date	Intensity	State
Aug 01 ~ Aug 24	-	Unborn
Aug 24 ~ Seq 01	$TD \Rightarrow H5$	Approaching USA
Sep 02	H5	Arriving at FL
Sep 04	H2	Arriving at GA
Sep 05	H3	Arriving at SC
Sep 05 ~ Sep 09	$H3 \Rightarrow ET$	Fading away

Table 2: Population mobility data description in three states, where NoC is the short of Number of Counties.

State	FL	GA	SC
Original NoC	67	159	46
Filter NoC	55	107	38
$Var(x_i^t)$	1.1011×10^{12}	6.9274×10^9	3.8356×10^{10}
$Var(x_{ij}^t)$	1.2892×10^8	8.9060×10^5	2.3480×10^7
$Max(x_i^t)$	6506832	596636	813207
$Q_{25}(x_i^t)$	46936	10755	31331
$Mean(x_i^t)$	648269	50373	160973

x_{ij}^t over the recovery period of T days. In the experiment, we observed that inter-regional population flows are significantly smaller compared to intra-regional flows, leading the model to overlook edge predictions. Therefore, the parameter λ is used to adjust the importance of edge predictions in our model. We use $AdamW$ [25] as our optimizer.

5 EXPERIMENT

5.1 Experimental Settings

5.1.1 Scenario. We select hurricane Dorian (2019) [34], which was delisted for the extensive damage it caused, as our disaster scenario. Dorian was born on August 24, 2019, then approached Florida (FL) and made landfall in FL on September 2nd, Georgia (GA) on September 4th, South Carolina (SC) on September 5th, and finally dissipated on September 9th, resulting in significant damage. Consequently, we conduct experiments in these three states. The temporal changes in hurricane Dorian's intensity and states are outlined in Table 1. *TD* and *ET* are short of "Tropical Depressions" and "Extratropical Transition", respectively, representing the beginning and end of Dorian in this scenario.

5.1.2 Dataset. The original population mobility data sourced from SafeGraph records the daily number of people moving between different Census Block Groups (CBGs) from August 1st to September 10th, 2019. We aggregate this inter-CBG daily mobility data by counties to construct the daily within-county population flows and between-county population flows, corresponding to the intra-regional population flows on nodes x_i^t and inter-regional population flows on edges x_{ij}^t. Based on the trajectory of Dorian, certain counties in these three states are located far from the hurricane's center. Therefore, we implement a county filtering process based on

weather conditions during Dorian and individually generate population mobility graphs for FL, GA, and SC. Detailed information about the county filtering process can be found in the Appendix.

The description of processed population mobility data is shown in Table 2, from which we can find that the variance of the intra-regional population flows x_i^t and the inter-regional population flows x_{ij}^t are huge. Besides, the highest recorded intra-regional population flows can reach 6,506,832 people in one day.

5.1.3 Metrics. We employ several metrics to evaluate the performance of our model, including Mean Absolute Error (**MAE**), Normalized Root-Mean-Square Error (**NRMSE**), and Coefficient of Determination ($\mathbf{R}^2$). **MAE** measures the average magnitude of the prediction errors. **NRMSE** is a dimensionless metric that normalizes the accuracy of a predictive model, accounting for the data variability:

$$NRMSE(x_i^t, \hat{x_i^t}) = \frac{\sqrt{\sum_{t=1}^{T} \sum_{i=1}^{n} (x_i^t - \hat{x_i^t})^2 / (T \times n)}}{\sqrt{\sum_{t=1}^{T} \sum_{i=1}^{n} (x_i^t - \bar{x})^2 / (T \times n)}}, \quad (22)$$

where $\bar{x}$ is the mean of the true values computed over all regions i and all times t, serving as the baseline for comparison. A lower **NRMSE** value indicates better model performance. $\mathbf{R}^2$ provides an unbiased measure of model quality, representing the proportion of the total variation in the dependent variable explained by the model. An $\mathbf{R}^2$ value closer to 1 indicates higher model performance.

5.1.4 Baseline. We compare our model CDGON with the following six classical baselines.

- **LSTM** [16] is a classic recurrent neural network designed to predict future sequences by learning patterns from historical data.
- **AGCRN** [1] combines GCN and Gated Recurrent Units (GRU) for dynamic graph prediction, enabling the adaptively learned graph structures.
- **NDCN** [50] focuses on capturing dynamics in complex networks with a Neural ODE designed with one GCN layer.
- **CG-ODE** [18] constructs temporal links between historical graphs and develops a Variational AutoEncoder(VAE)-based model to capture the co-evolution of nodes and edges using coupled Neural ODE functions.
- **STG-NCDE** [10] employs Neural Controlled Differential Equations (NCDE), incorporating trajectory gradients $\frac{dX(t)}{dt}$ generated through the natural cubic spline of original signals.
- **PatchTST** [28] divides historical sequences into a series of equal-length patches, then develops a transformer-based model to predict the trajectories of multivariate data.

5.2 Performance Evaluation

We assess the performance of different models in each of the three states individually. Due to the nature of our CDGON model, in addition to the initial abnormal population mobility graph on the day Dorian arrived, CDGON requires the normal intra-regional population flow prior to the disaster as input. During training, several post-disaster graph snapshots are needed as labels. Consequently, the dynamic graphs in the recovery process are divided into two parts: the former for training and the latter for testing.

Table 3: Performance comparison of our model and baselines on three states for predicting the recovery process of intra-regional population flows, where lower NRMSE and MAE, higher R^2 are better. Bold denotes best results.

Model	Region	FL			GA			SC		
	Metrics	MAE	NRMSE	R^2	MAE	NRMSE	R^2	MAE	NRMSE	R^2
LSTM		302884.0938	0.6689	0.5526	27099.3320	0.8700	0.2431	45117.3867	0.4089	0.8328
AGCRN		273478.9062	0.5377	0.7109	26782.4121	0.9181	0.1570	22293.4277	0.1938	0.9624
NDCN		406064.2812	0.3987	0.8411	11569.9785	0.3539	0.8747	94850.3906	0.6801	0.5375
CG-ODE		224787.1250	0.2936	0.9138	13370.4551	0.2664	0.9290	89249.2109	0.7564	0.4279
STG-NCDE		226016.1562	0.6683	0.5533	5938.1401	0.2316	0.9463	13173.6650	0.2074	0.9570
PatchTST		96736.0547	0.1632	0.9734	3108.3894	0.0963	0.9907	12399.1855	0.1347	0.9819
CDGON		**59767.4805**	**0.0724**	**0.9948**	**2013.2821**	**0.0475**	**0.9977**	**9040.6758**	**0.0771**	**0.9941**

Table 4: Performance comparison of our model and baselines on three states for predicting the recovery process of inter-regional population flows, where bold denotes best results.

Region	Metrics	CG-ODE	STG-NCDE	CDGON
FL	NRMSE	1.0051	0.7603	**0.4364**
	R^2	-0.0103	0.4218	**0.8096**
GA	NRMSE	**0.0241**	0.5031	0.2663
	R^2	**0.9879**	0.7468	0.9291
SC	NRMSE	-0.5193	**0.4718**	0.6086
	R^2	1.2326	**0.7773**	0.6296

Based on our observation of the human mobility curve during hurricane Dorian, whose details are presented in the Appendix, we note that it takes approximately four days for the intra-regional population flow of all counties to return to normal, excluding the day Dorian arrived. Therefore, we use the first three dynamic graphs after disaster for training and the fourth dynamic graph for testing. For example, Dorian arrived in FL on September 2nd, causing a sharp decrease in population mobility on that day, followed by recovery over the next four days. CDGON takes the population mobility graph of FL on September 2nd and the normal intra-regional flows as input. It is trained on the data from September 3rd to 5th, and is evaluated on the graph from September 6th. For Georgia (GA) and South Carolina (SC), the testing is conducted on the population mobility graph from September 8th and 9th, respectively.

The experimental results for predicting the intra-regional population flow for all models are presented in Table 3, while the results for inter-regional population flow are shown in Table 4. Notably, our CDGON model consistently demonstrates superior predictive performance in predicting intra-regional population flows among all scenarios. For the prediction of inter-regional population flows, although CDGON does not outperform baselines in all situations, it is still the most stable and partially optimal compared with baseline models. Furthermore, Fig. 3 vividly illustrates the predictive performance comparison between our model and STG-NCDE on the fourth day after Dorian's arrival. This visualization highlights that our model produces accurate predictions that closely align with the ground truth, surpassing STG-NCDE.
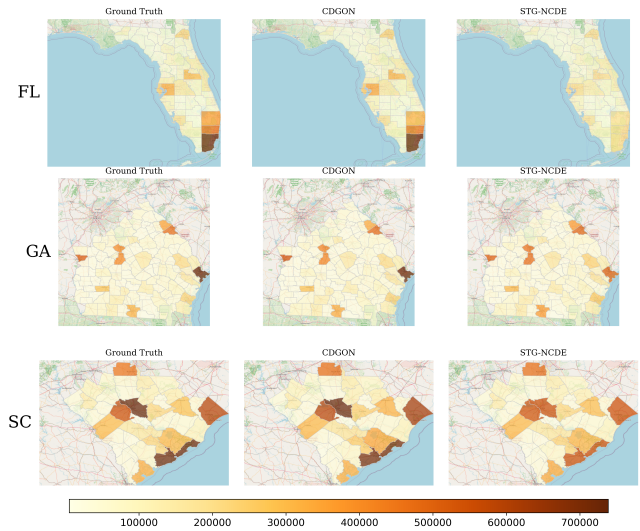

Figure 3: Intra-regional population flow visualizations in three states among ground truth and prediction results from CDGON and STG-NCDE.
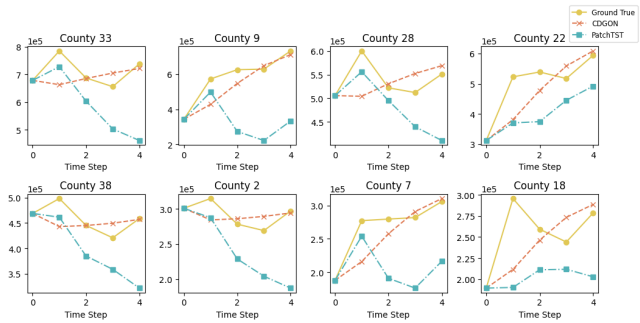

Figure 4: Intra-regional population flow prediction in the 8 counties with the largest population in SC state, where the two predictive curves are generated by the models trained in FL.

Table 5: Performance comparison for predicting intra-regional population flow recovery process in each state by the model trained on other two states, where lower NRMSE and MAE, higher R^2 are better. Bold denotes best results. Models with * can not be generalized to different states due to their requirement of the same graph structure, thus their prediction performance results come from training and testing in the target city simultaneously.

Source → Target	Metrics	LSTM*	AGCRN*	NDCN	CG-ODE*	STG-NCDE*	PatchTST	CDGON
FL → GA	MAE	30069.4746	27000.6348	24600.7168	24787.2109	7720.2603	**4872.3203**	5433.7192
	NRMSE	0.9254	0.9031	0.5628	0.6689	0.3452	0.1444	**0.1301**
	R^2	0.1436	0.1843	0.6832	0.5526	0.8808	0.9791	**0.9831**
FL → SC	MAE	46591.9336	23959.2617	57581.6367	124385.3672	15826.1348	38007.8047	**13609.5889**
	NRMSE	0.4129	0.2143	0.4980	0.9807	0.1964	0.4144	**0.1508**
	R^2	0.8295	0.9541	0.7520	0.0382	0.9614	0.8283	**0.9773**
GA → FL	MAE	314732.8125	110829.3672	89669.6328	308634.5938	205125.8438	70575.5312	**48276.1992**
	NRMSE	0.6675	0.2074	0.1889	0.5605	0.6711	0.1536	**0.0997**
	R^2	0.5544	0.9570	0.9643	0.6858	0.5496	0.9764	**0.9901**
GA → SC	MAE	46591.9336	23959.2617	37860.0586	124385.3672	15826.1348	16386.5156	**14315.9375**
	NRMSE	0.4129	0.2143	0.3880	0.9807	0.1964	0.1844	**0.1341**
	R^2	0.8295	0.9541	0.8495	0.0382	0.9614	0.9660	**0.9820**
SC → FL	MAE	314732.8125	110829.3672	1353806.5000	308634.5938	205125.8438	100522.4141	**73204.6719**
	NRMSE	0.6675	0.2074	1.4442	0.5605	0.6711	0.2294	**0.1412**
	R^2	0.5544	0.9570	-1.0858	0.6858	0.5496	0.9474	**0.9801**
SC → GA	MAE	30069.4746	27000.6348	334504.1250	24787.2109	7720.2603	**5576.4810**	8921.1035
	NRMSE	0.9254	0.9031	5.1555	0.6689	0.3452	0.2232	**0.1770**
	R^2	0.1436	0.1843	-25.5788	0.5526	0.8808	0.9502	**0.9687**

5.3 Generalization

To verify the model's generalization ability, we train our model on each state (source state), and apply the trained model to the other two states (target states), denoted as "source → target". Specifically, we use all the dynamic population mobility graphs during the recovery process of the source state to train our model. The trained model is then applied to predict the entire recovery processes of the other two target states, differing from the training setting in Table 3.

The performance of generalization is shown in Table 5, where the predictive performance of our CDGON is consistently optimal. This outcome demonstrates the generalization capability of CDGON. Such accurate predictions hold substantial significance for devising coordinated post-disaster recovery plans spanning multiple states. From the comparison with PatchTST in Fig. 4, our CDGON can predict the intra-regional flows with higher accuracy. Although there is some disparity between our predictions and the real values from the visualization, achieving such accuracy by only knowing the initial state and normal state illustrates the potential of our model.

5.4 Hyper-parameters Setting

The main hyper-parameters used in our CDGON model include embedding dimension, edge loss weight (λ) in Eq. (21), and learning rate. These parameters were set to 48, 100, and 0.003, respectively. Notably, we found that setting the embedding dimension to 64, while keeping the other two parameters unchanged, results in the best performance in the generalization part but underperforms in

the evaluation part. This indicates the potential of our CDGON's generalization ability. However, to achieve balanced performance between evaluation and generalization, we used 48 as our embedding dimension.

5.5 Ablation Study

To assess the efficacy of different components in the design of our CDGON, we conducted ablation experiments across three aspects:

- **w/o PIDM**: CDGON without PIDM, utilizing a linear layer to learn from the node embeddings directly.
- **w/o GCN-α**: CDGON without GCN to compute the α_i^t, employing a linear layer to compute it directly from z_i^t.
- **w/o NEIM**: CDGON without NEIM, focusing solely on the PIDM in node ODE function and changing the edge ODE function to only consider self-evolution.

The results of the ablation study are presented in Table 6. This comprehensive assessment includes the evaluation of the predictive performance both in the nodes and edges. This experiment indicates that the removal of any of the mentioned modules results in a reduction of our model's predictive ability on intra-regional population flows. Moreover, our models' performance on inter-regional population flows significantly deteriorates when any designed module is removed. These findings fully illustrate the effectiveness of our model design.

Table 6: Ablation study for different components of our model on three states, where lower NRMSE and MAE, higher R^2 are better. Bold denotes best results. Node and Edge represent two types of evaluation implemented on the recovery process of intra-regional population flows and inter-regional population flows respectively.

Model	Region	FL			GA			SC		
	Metrics	MAE	NRMSE	R^2	MAE	NRMSE	R^2	MAE	NRMSE	R^2
CDGON	Node	59767.4805	0.0724	0.9948	**2013.2821**	**0.0475**	**0.9977**	**9040.6758**	**0.0771**	**0.9941**
	Edge	**1934.2816**	**0.4364**	**0.8096**	48.2338	0.2663	0.9291	714.8368	0.6086	0.6296
w/o PIDM	Node	60685.7891	0.1002	0.9900	9389.4014	0.3432	0.8822	36499.0273	0.4174	0.8258
	Edge	1945.6016	0.1002	1.0087	89.7465	1.0087	-0.0176	801.9778	1.0142	-0.0285
w/o GCN-α	Node	73036.6641	0.1185	0.9860	6143.5601	0.1921	0.9631	17583.4277	0.1828	0.9666
	Edge	1945.6016	0.1002	1.0087	89.7465	1.0087	-0.0176	801.9778	1.0142	-0.0285
w/o NEIM	Node	**30396.2402**	**0.0570**	**0.9968**	6783.2905	0.9630	0.1925	25347.1289	0.2261	0.9489
	Edge	1945.6016	0.1002	1.0087	89.7465	1.0087	-0.0176	801.9778	1.0142	-0.0285

6 RELATED WORK

Urban Mobility Recovery Dynamic Modeling. Traditional studies on modeling and analyzing the recovery dynamics of urban population mobility often adopt mathematical approaches to understand and unveil patterns in population movement after disasters. For example, the more socially connected a community is to other communities, the faster it will recover after a disaster [47]. Additionally, socioeconomic and racial disparities affect the resilience capacity [17], and the perturbed population mobility post-disaster is highly correlated with steady mobility state [38]. Modeling methods vary for different mobility metrics [23, 37, 38, 43, 45], but the basic recovery trend can be identified [20, 46]. These studies on the recovery dynamics of urban mobility is also part of resilience research in complex networks [11, 13].

Physic-informed Neural ODE. Incorporating physic-based knowledge into the data-driven method can significantly improve method performance in various scenarios, such as sensor calibration [35], field reconstruction [26, 33], air pollution estimation [7–9] and crowd simulation [2]. Neural ODE can also be applied in various fields by integrating domain knowledge, such as structural health monitoring [22], trajectory forecasting for multi-object physical systems [24, 40, 41], turbulent fluid dynamic [32] and complex climate systems [19, 27]. Incorporating physics-based knowledge will lead to a high physical interpretability. Liu et al. [24] present the Physics-informed Neural Graph ODE (PINGO) model, utilizing Newton's second law to simulate long-term dynamics of multi-object physical systems. Roehrl et al. [31] integrate the equations of motion in Lagrange mechanics to Neural ODE to simulate the movement of a cart pole.

Post-disaster Emergency Management. In recent years, technological advancements have significantly enhanced the efficiency and effectiveness of post-disaster emergency management. Accurate prediction of post-disaster urban mobility recovery is crucial for various emergency management activities. For example, Ren et al. [30] propose a reinforcement learning method for scheduling UAV swarms for data communication, which can assist in the restoration of damaged communication networks effectively based on the accurate mobility recovery prediction. Furthermore, in severely affected areas with slow population mobility recovery,

existing routes may be destroyed. Thus, opening new transportation routes to these detected areas is vital. To address this issue, Jian et al. [21] utilize wheeled robots for path generation on vegetated terrain, and Wang et al. [36] also achieve navigation in the harsh environment using UAVs. Accurate predictions also prove invaluable in emergency resource allocation. In complex environments, drones can efficiently deliver essential resources [4, 5]. For example, after a forest fire, residual fires in remote areas can be effectively suppressed through the collaborative scheduling of multiple UAVs [6]. By combining our CDGON with these algorithms, the post-disaster reconstruction work can be better carried out.

7 CONCLUSION

In this paper, we investigate the dynamic urban population mobility prediction problem in post-disaster scenarios by proposing a novel Neural ODE model. Informed by physics-based knowledge from the ST Decay Model, our proposed model CDGON can capture the co-evolving process of intra-regional and inter-regional population flows, enhancing the prediction of urban population mobility after extreme events. Extensive experiments on three real-world mobility datasets demonstrate the superiority of our model in forecasting the recovery trajectory of urban population mobility. Our code and data are available at: https://github.com/tsinghua-fib-lab/CDGON-KDD24.

In future work, we will explore incorporating the normal inter-regional flows to further improve prediction performance. Furthermore, we aim to extend the predictions to other types of disasters (e.g., epidemics, winter storms, etc.). With the rise of the large language model, more researchers focus on using the generative pre-trained models to solve the spatio-temporal prediction problem [48, 49], which can combine with CDGON to enhance its generalization capability to predict post-disaster population mobility.

REFERENCES

[1] Lei Bai, Lina Yao, Can Li, Xianzhi Wang, and Can Wang. 2020. Adaptive graph convolutional recurrent network for traffic forecasting. *Advances in neural information processing systems* 33 (2020), 17804–17815.

[2] Hongyi Chen, Jingtao Ding, Yong Li, Yue Wang, and Xiao-Ping Zhang. 2024. Social physics informed diffusion model for crowd simulation. *arXiv preprint arXiv:2402.06680* (2024).

[3] Ricky TQ Chen, Yulia Rubanova, Jesse Bettencourt, and David K Duvenaud. 2018. Neural ordinary differential equations. *Advances in neural information processing systems* 31 (2018).

[4] Xinlei Chen, Aveek Purohit, Shijia Pan, Carlos Ruiz, Jun Han, Zheng Sun, Frank Mokaya, Patric Tague, and Pei Zhang. 2017. Design experiences in minimalistic flying sensor node platform through sensorfly. *ACM Transactions on Sensor Networks (TOSN)* 13, 4 (2017), 1–37.

[5] Xuecheng Chen, Haoyang Wang, Zuxin Li, Wenbo Ding, Fan Dang, Chengye Wu, and Xinlei Chen. 2022. DeliverSense: Efficient delivery drone scheduling for crowdsensing with deep reinforcement learning. In *Adjunct Proceedings of the 2022 ACM International Joint Conference on Pervasive and Ubiquitous Computing and the 2022 ACM International Symposium on Wearable Computers*. 403–408.

[6] Xuecheng Chen, Zijian Xiao, Yuhan Cheng, ChenChun Hsia, Haoyang Wang, Jingao Xu, Susu Xu, Fan Dang, Xiao-Ping Zhang, Yunhao Liu, et al. 2024. SOScheduler: Toward Proactive and Adaptive Wildfire Suppression via Multi-UAV Collaborative Scheduling. *IEEE Internet of Things Journal* (2024).

[7] Xinlei Chen, Susu Xu, Xinyu Liu, Xiangxiang Xu, Hae Young Noh, Lin Zhang, and Pei Zhang. 2020. Adaptive hybrid model-enabled sensing system (HMSS) for mobile fine-grained air pollution estimation. *IEEE Transactions on Mobile Computing* 21, 6 (2020), 1927–1944.

[8] Xinlei Chen, Xiangxiang Xu, Xinyu Liu, Hae Young Noh, Lin Zhang, and Pei Zhang. 2016. Hap: Fine-grained dynamic air pollution map reconstruction by hybrid adaptive particle filter. In *Proceedings of the 14th ACM Conference on Embedded Network Sensor Systems CD-ROM*. 336–337.

[9] Xinlei Chen, Xiangxiang Xu, Xinyu Liu, Shijia Pan, Jiayou He, Hae Young Noh, Lin Zhang, and Pei Zhang. 2018. Pga: Physics guided and adaptive approach for mobile fine-grained air pollution estimation. In *Proceedings of the 2018 ACM International Joint Conference and 2018 International Symposium on Pervasive and Ubiquitous Computing and Wearable Computers*. 1321–1330.

[10] Jeongwhan Choi, Hwangyong Choi, Jeehyun Hwang, and Noseong Park. 2022. Graph neural controlled differential equations for traffic forecasting. In *Proceedings of the AAAI Conference on Artificial Intelligence*, Vol. 36. 6367–6374.

[11] Jingtao Ding, Chang Liu, Yu Zheng, Yunke Zhang, Zihan Yu, Ruikun Li, Hongyi Chen, Jinghua Piao, Huandong Wang, Jiazhen Liu, et al. 2024. Artificial Intelligence for Complex Network: Potential, Methodology and Application. *arXiv preprint arXiv:2402.16887* (2024).

[12] Zheng Fang, Qingqing Long, Guojie Song, and Kunqing Xie. 2021. Spatial-temporal graph ode networks for traffic flow forecasting. In *Proceedings of the 27th ACM SIGKDD conference on knowledge discovery & data mining*. 364–373.

[13] Jianxi Gao, Baruch Barzel, and Albert-László Barabási. 2016. Universal resilience patterns in complex networks. *Nature* 530, 7590 (2016), 307–312.

[14] Masahiko Haraguchi, Akihiko Nishino, Akira Kodaka, Maura Allaire, Upmanu Lall, Liao Kuei-Hsien, Kaya Onda, Kota Tsubouchi, and Naohiko Kohtake. 2022. Human mobility data and analysis for urban resilience: A systematic review. *Environment and Planning B: Urban Analytics and City Science* 49, 5 (2022), 1507–1535.

[15] Kaiming He, Xiangyu Zhang, Shaoqing Ren, and Jian Sun. 2016. Deep residual learning for image recognition. In *Proceedings of the IEEE conference on computer vision and pattern recognition*. 770–778.

[16] Sepp Hochreiter and Jürgen Schmidhuber. 1997. Long Short-Term Memory. 9, 8 (1997), 1735–1780. Conference Name: Neural Computation.

[17] Boyeong Hong, Bartosz J Bonczak, Arpit Gupta, and Constantine E Kontokosta. 2021. Measuring inequality in community resilience to natural disasters using large-scale mobility data. *Nature communications* 12, 1 (2021), 1870.

[18] Zijie Huang, Yizhou Sun, and Wei Wang. 2021. Coupled graph ode for learning interacting system dynamics. In *Proceedings of the 27th ACM SIGKDD Conference on Knowledge Discovery & Data Mining*. 705–715.

[19] Jeehyun Hwang, Jeongwhan Choi, Hwangyong Choi, Kookjin Lee, Dongeun Lee, and Noseong Park. 2021. Climate modeling with neural diffusion equations. In *2021 IEEE International Conference on Data Mining (ICDM)*. IEEE, 230–239.

[20] Tasnuba Binte Jamal and Samiul Hasan. 2023. Understanding the Loss in Community Resilience due to Hurricanes using Facebook Data. *arXiv preprint arXiv:2302.03530* (2023).

[21] Zhuozhu Jian, Zejia Liu, Haoyu Shao, Xueqian Wang, Xinlei Chen, and Bin Liang. 2023. Path Generation for Wheeled Robots Autonomous Navigation on Vegetated Terrain. *IEEE Robotics and Automation Letters* (2023).

[22] Zhilu Lai, Wei Liu, Xudong Jian, Kiran Bacsa, Limin Sun, and Eleni Chatzi. 2022. Neural modal ordinary differential equations: Integrating physics-based modeling with neural ordinary differential equations for modeling high-dimensional monitored structures. *arXiv preprint arXiv:2207.07883* (2022).

[23] Weiyu Li, Qi Wang, Yuanyuan Liu, Mario L Small, and Jianxi Gao. 2022. A spatiotemporal decay model of human mobility when facing large-scale crises. *Proceedings of the National Academy of Sciences* 119, 33 (2022), e2203042119.

[24] Yang Liu, Jiashun Cheng, Haihong Zhao, Tingyang Xu, Peilin Zhao, Fugee Tsung, Jia Li, and Yu Rong. 2023. Physics-Inspired Neural Graph ODE for Long-term Dynamical Simulation. *arXiv preprint arXiv:2308.13212* (2023).

[25] Ilya Loshchilov and Frank Hutter. 2017. Decoupled weight decay regularization. *arXiv preprint arXiv:1711.05101* (2017).

[26] Ji Luo, Yiling Hu, Chengzhao Yu, Chaopeng Hong, Xiao-Ping Zhang, and Xinlei Chen. 2023. Field Reconstruction-Based Non-Rendezvous Calibration for Low Cost Mobile Sensors. In *Adjunct Proceedings of the 2023 ACM International Joint Conference on Pervasive and Ubiquitous Computing & the 2023 ACM International Symposium on Wearable Computing*. 688–693.

[27] Björn Lütjens, Catherine H Crawford, Mark Veillette, and Dava Newman. 2021. Pce-pinns: Physics-informed neural networks for uncertainty propagation in ocean modeling. *arXiv preprint arXiv:2105.02939* (2021).

[28] Yuqi Nie, Nam H Nguyen, Phanwadee Sinthong, and Jayant Kalagnanam. 2022. A time series is worth 64 words: Long-term forecasting with transformers. *arXiv preprint arXiv:2211.14730* (2022).

[29] Michael Poli, Stefano Massaroli, Junyoung Park, Atsushi Yamashita, Hajime Asama, and Jinkyoo Park. 2019. Graph neural ordinary differential equations. *arXiv preprint arXiv:1911.07532* (2019).

[30] Jiyuan Ren, Yanggang Xu, Zuxin Li, Chaopeng Hong, Xiao-Ping Zhang, and Xinlei Chen. 2023. Scheduling UAV Swarm with Attention-based Graph Reinforcement Learning for Ground-to-air Heterogeneous Data Communication. In *Adjunct Proceedings of the 2023 ACM International Joint Conference on Pervasive and Ubiquitous Computing & the 2023 ACM International Symposium on Wearable Computing*. 670–675.

[31] Manuel A Roehrl, Thomas A Runkler, Veronika Brandtstetter, Michel Tokic, and Stefan Obermayer. 2020. Modeling system dynamics with physics-informed neural networks based on Lagrangian mechanics. *IFAC-PapersOnLine* 53, 2 (2020), 9195–9200.

[32] Varun Shankar, Christopher Rackauckas, and Venkatasubramanian Viswanathan. 2020. Learning non-linear spatio-temporal dynamics with convolutional Neural ODEs. *Advances in neural information processing systems*.

[33] Yifei Sun, Yuxuan Liu, Ziteng Wang, Xiaolei Qu, Dezhi Zheng, and Xinlei Chen. 2022. C-RIDGE: Indoor CO2 Data Collection System for Large Venues Based on prior Knowledge. In *Proceedings of the 20th ACM Conference on Embedded Networked Sensor Systems*. 1077–1082.

[34] NOAA US Department of Commerce. 2019. *Hurricane Dorian, September 6, 2019*. https://www.weather.gov/mhx/Dorian2019 Publisher: NOAA's National Weather Service.

[35] Haoyang Wang, Yuxuan Liu, Chenyu Zhao, Jiayou He, Wenbo Ding, and Xinlei Chen. 2023. CaliFormer: Leveraging Unlabeled Measurements to Calibrate Sensors with Self-supervised Learning. In *Adjunct Proceedings of the 2023 ACM International Joint Conference on Pervasive and Ubiquitous Computing & the 2023 ACM International Symposium on Wearable Computing*. 743–748.

[36] Haoyang Wang, Jingao Xu, Chenyu Zhao, Zihong Lu, Yuhan Cheng, Xuecheng Chen, Xiao-Ping Zhang, Yunhao Liu, and Xinlei Chen. 2024. TransformLoc: Transforming MAVs into Mobile Localization Infrastructures in Heterogeneous Swarms. *arXiv preprint arXiv:2403.08815* (2024).

[37] Qi Wang and John E Taylor. 2015. Resilience of human mobility under the influence of typhoons. *Procedia engineering* 118 (2015), 942–949.

[38] Qi Wang and John E Taylor. 2016. Patterns and limitations of urban human mobility resilience under the influence of multiple types of natural disaster. *PLoS one* 11, 1 (2016), e0147299.

[39] Ruoxi Wang, Qi Wang, and Nan Li. 2023. Percolation transitions in urban mobility networks in America's 50 largest cities. *Sustainable Cities and Society* 91 (2023), 104435.

[40] Song Wen, Hao Wang, Di Liu, Qilong Zhangli, and Dimitris Metaxas. 2024. Second-Order Graph ODEs for Multi-Agent Trajectory Forecasting. In *Proceedings of the IEEE/CVF Winter Conference on Applications of Computer Vision*. 5101–5110.

[41] Song Wen, Hao Wang, and Dimitris Metaxas. 2022. Social ode: Multi-agent trajectory forecasting with neural ordinary differential equations. In *European Conference on Computer Vision*. Springer, 217–233.

[42] Jared Willard, Xiaowei Jia, Shaoming Xu, Michael Steinbach, and Vipin Kumar. 2022. Integrating scientific knowledge with machine learning for engineering and environmental systems. *Comput. Surveys* 55, 4 (2022), 1–37.

[43] Takahiro Yabe, P Suresh C Rao, and Satish V Ukkusuri. 2021. Resilience of interdependent urban socio-physical systems using large-scale mobility data: Modeling recovery dynamics. *Sustainable Cities and Society* 75 (2021), 103237.

[44] Takahiro Yabe, P Suresh C Rao, Satish V Ukkusuri, and Susan L Cutter. 2022. Toward data-driven, dynamical complex systems approaches to disaster resilience. *Proceedings of the National Academy of Sciences* 119, 8 (2022), e2111997119.

[45] Takahiro Yabe, Kota Tsubouchi, Naoya Fujiwara, Yoshihide Sekimoto, and Satish V Ukkusuri. 2019. Universality of population recovery patterns after disasters. *arXiv preprint arXiv:1905.01804* (2019).

[46] Takahiro Yabe, Kota Tsubouchi, Naoya Fujiwara, Yoshihide Sekimoto, and Satish V Ukkusuri. 2020. Understanding post-disaster population recovery patterns. *Journal of the Royal Society Interface* 17, 163 (2020), 20190532.

[47] Takahiro Yabe, Satish V Ukkusuri, and P Suresh C. Rao. 2019. Mobile phone data reveals the importance of pre-disaster inter-city social ties for recovery after hurricane maria. *Applied Network Science* 4, 1 (2019), 98.

[48] Yuan Yuan, Jingtao Ding, Jie Feng, Depeng Jin, and Yong Li. 2024. UniST: A Prompt-Empowered Universal Model for Urban Spatio-Temporal Prediction. *arXiv preprint arXiv:2402.11838* (2024).

[49] Yuan Yuan, Chenyang Shao, Jingtao Ding, Depeng Jin, and Yong Li. 2024. A Generative Pre-Training Framework for Spatio-Temporal Graph Transfer Learning. *arXiv preprint arXiv:2402.11922* (2024).

[50] Chengxi Zang and Fei Wang. 2020. Neural dynamics on complex networks. In *Proceedings of the 26th ACM SIGKDD international conference on knowledge discovery & data mining*. 892–902.

A PROOFS OF THE THEOREMS

Theorem 1. *Denote $r_i(t)$ as the abnormal intra-regional population flow of region i after a disaster, which is described in the ST Decay Model shown in Eq. (1). The derivative of $r_i(t)$ satisfies the following differential equation:*

$$\frac{\mathrm{d}r_i(t)}{\mathrm{d}t} = \alpha \frac{r_i(t)}{\overline{r_i}}[\overline{r_i} - r_i(t)], \tag{23}$$

where α indicates the decay coefficientand this implies that $r_i(t)$ will approach to the normal intra-regional population flow $\overline{r_i}$ over time governed by α.

PROOF. First, the original spatiotemporal decay model can be differentiated into:

$$\frac{\mathrm{d}r_i(t)}{\mathrm{d}t} = -\overline{r_i} \frac{\left(k(t)\sum_{j=1}^{L} w_{ij}N_j(t)\right)'}{(1 + k(t)\sum_{j=1}^{L} w_{ij}N_j(t))^2}, \tag{24}$$

which cannot be solved at this time for unknown functions $k(t)$ and $N_j(t)$. However, an interesting observation can be found as follows:

The spatial decay $\sum_{j=1}^{L} w_{ij}N_j(t)$ in Eq. (1), which represents the total severity of a disaster to the neighbors of the region i, actually will weaken over time after a disaster. Therefore, it is reasonable to assume the whole $k(t)\sum_{j=1}^{L} w_{ij}N_j(t)$ decays over time. Consequently, the negative exponential function $k_0e^{-\alpha t}$, which is observed [23] as the most accurate function to describe the spatiotemporal decay process, is used in this paper to replace $k(t)\sum_{j=1}^{L} w_{ij}N_j(t)$:

$$k(t)\sum_{j=1}^{L} w_{ij}N_j(t) = k_0e^{-\alpha t}, \tag{25}$$

where α is the decay control parameters and k_0 is the initial rate of change in mobility behavior.

Accordingly, a new decay model is generated:

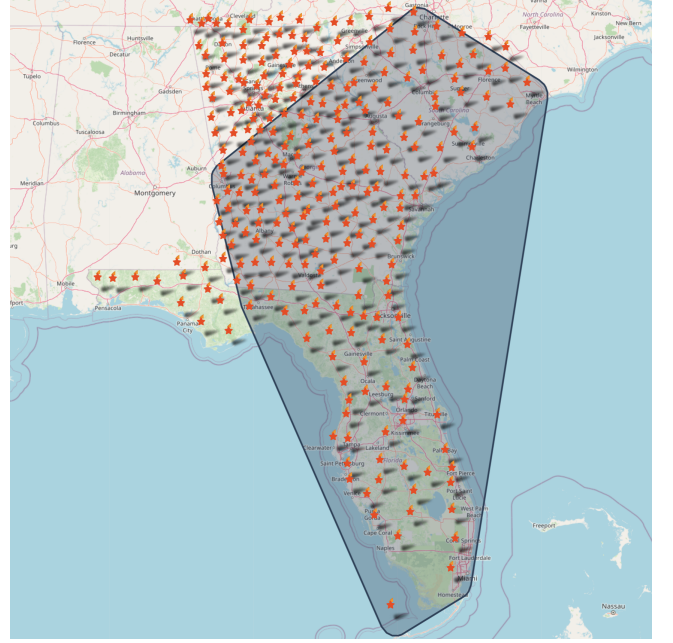$$r_i(t) = \frac{\overline{r_i}}{1 + k_0e^{-\alpha t}}, \tag{26}$$

Figure 5: County filtering result, where a star represents a county and the constructed convex hull is the black transparent

which can be differentiated over time t to:

$$\begin{aligned}
\frac{\mathrm{d}r_i(t)}{\mathrm{d}t} &= -\overline{r_i} \frac{(k_0e^{-\alpha t})'}{(1 + k_0e^{-\alpha t})^2} \\
&= -\overline{r_i} \frac{-\alpha k_0e^{-\alpha t}}{\left(\frac{\overline{r_i}}{r_i(t)}\right)^2} \\
&= \alpha\overline{r_i} \frac{\frac{\overline{r_i}}{r_i(t)} - 1}{\left(\frac{\overline{r_i}}{r_i(t)}\right)^2} \\
&= \alpha \frac{r_i(t)}{\overline{r_i}}[\overline{r_i} - r_i(t)],
\end{aligned} \tag{27}$$

which proves the theorem.

□

B COUNTY FILTERING

We utilize daily wind speed and precipitation data recorded by weather stations in FL, GA, and SC. We allocate weather stations to each county based on the longitude and latitude bounds of each county, and average the wind speed and precipitation recorded by these stations to obtain the values for each county. We retain counties where the wind speed and precipitation exceed a certain threshold, indicating a significant impact on normal life. However, we found that some states are relatively small and do not have weather stations nearby allocatable. Expanding their longitude and latitude bounds does not resolve this issue. As a result, the selected counties cannot well represent the real population mobility of this area. To address this issue, we constructed a convex hull based on
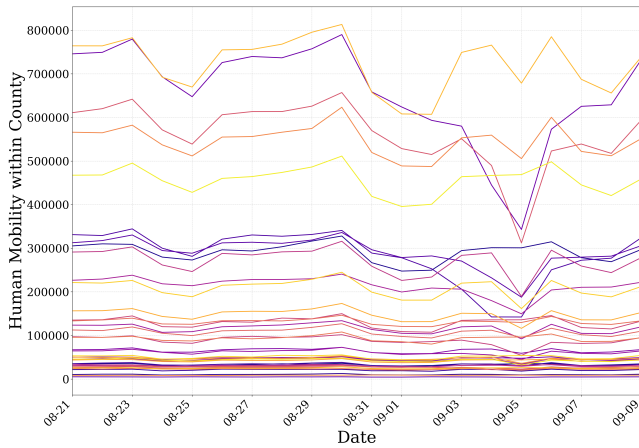
Figure 8: Human mobility within each county time in South Carolina, where a line is the within-county population flow curve of a county, and different colors represent different counties
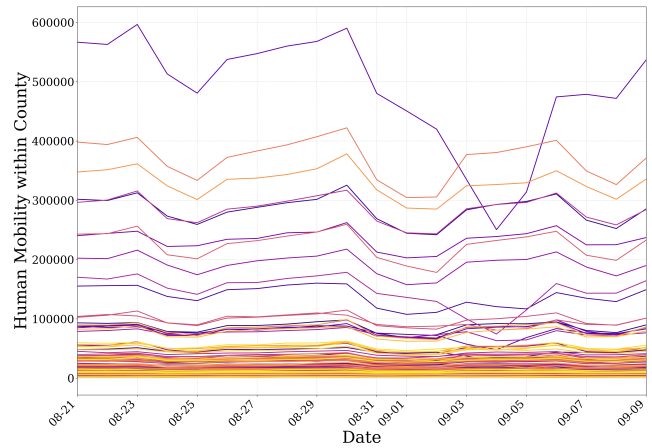

Figure 7: Human mobility within each county over time in Georgia, where a line is the within-county population flow curve of a county, and different colors represent different counties
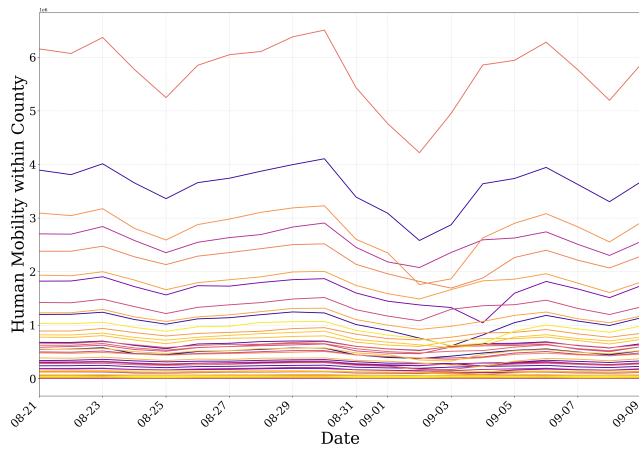
the existing counties and retained the counties within this range. The filtering results for FL, GA, and SC are shown in Fig. 5.

C POPULATION MOBILITY CURVES IN DIFFERENT COUNTIES BEFORE AND AFTER DORIAN

To better illustrate the complexity of the population mobility recovery process and provide a better understanding of the population mobility recovery process, the human mobility curves ranging from August 21st to September 9th of FL, GA, and SC are provided in Fig. 6, Fig. 7, and Fig. 8, respectively, which differs from Fig. 1.

Figure 6: Human mobility within each county over time in Florida, where a line is the within-county population flow curve of a county, and different colors represent different counties.